Check for updates

Angewandte Chemie International Edition

Angewandte International Edition Chemie

GDCh German Chemical Society

How to cite: *Angew. Chem. Int. Ed.* **2026**, 65, e24756
doi.org/10.1002/anie.202524756

RESEARCH ARTICLE

Near-Infrared-Activated Multiphoton Photocatalytic System for Synergistic Therapy via CO Generation and •OH Production

Bo Li[1] | Yunyang Qian[2] | Xiyuan Zhang[2] | Xin Lu[1] | Yifan Huang[3] | Xianshun Sun[1] | Hongping Zhou[1] | Yupeng Tian[1] | Dandan Li[1] | Hai-Long Jiang[2,3]

[1]Institutes of Physical Science and Information Technology, School of Chemistry and Chemical Engineering, Key Laboratory of Structure and Functional Regulation of Hybrid Materials, Ministry of Education, Anhui University, Hefei, P.R. China | [2]Hefei National Research Center for Physical Sciences At the Microscale, College of Chemistry and Materials Science, University of Science and Technology of China, Hefei, P.R. China | [3]Department of Radiation Oncology, The First Affiliated Hospital of USTC, Division of Life Sciences and Medicine, University of Science and Technology of China, Hefei, P.R. China

Correspondence: Xianshun Sun (sxshun@ahu.edu.cn) | Dandan Li (chemlidd@163.com) | Hai-Long Jiang (jianglab@ustc.edu.cn)

Received: 10 November 2025 | **Revised:** 31 December 2025 | **Accepted:** 21 January 2026

Keywords: metal-organic frameworks | multiphoton photocatalytic | Photocatalytic CO_2 reduction | tumor therapy

ABSTRACT

Light-triggered controllable carbon monoxide (CO) release represents a promising approach for cancer therapy but is limited by the poor tissue penetration of light and insufficient CO release rates within deep tumor microenvironments. Herein, inspired by near-infrared (NIR)-activated multiphoton photocatalysis, a novel zinc-based metal-organic framework (ZnTBH) is reported, for the first time, to enable effective NIR-mediated synergistic therapy through combined CO gas therapy and photodynamic therapy (PDT) in deep-seated tumors. The engineered MOF integrates a V-shaped Tröger's base (TB) derivative with an A-π-A configuration as the organic linker, synergistically enhancing CO_2 adsorption to overcome the "dilute CO_2" challenge in tumors while enabling efficient endogenous CO_2-to-CO conversion via NIR-driven multiphoton photocatalysis. Moreover, the photogenerated holes localize on biphenyl-4,4'-dicarboxylic acid can drive water oxidation to hydroxyl radicals (•OH), thereby further improving therapeutic efficacy. This study presents a significant advancement in the design of NIR light-driven photocatalytic systems for safe, precise, and localized CO delivery, offering new opportunities for CO-based or combination therapies in the treatment of deep-seated tumors.

1 | Introduction

Carbon monoxide (CO), once regarded merely as a toxic gas, has emerged as a crucial gaseous signaling molecule involved in diverse physiological and pathological processes [1–3]. In oncology, CO exhibits notable anti-tumor effects by disrupting the mitochondrial respiratory chain, altering reactive oxygen species (ROS) levels, suppressing DNA repair, and inhibiting anti-apoptotic proteins [4–9]. Despite its therapeutic potential, conventional CO delivery strategies, primarily based on transition metal carbonyl compounds (e.g., $[Mn_2(CO)_{10}]$, $[RuCl_2(CO)_3]_2$), or biomacromolecule-based nanoparticles, face significant limitations. These systems often fail to achieve sustained and controllable CO release at the target site, thereby hampering therapeutic efficacy [10–13]. To address these limitations, photocatalytic CO_2 reduction has emerged as an innovative strategy for in situ CO generation. This approach exploits the elevated CO_2 levels in the tumor microenvironment ($pCO_2 \approx 80$ mmHg, significantly higher than in normal tissues) as an endogenous substrate for catalytic CO production [14–16]. However, most current photocatalytic

© 2026 Wiley-VCH GmbH

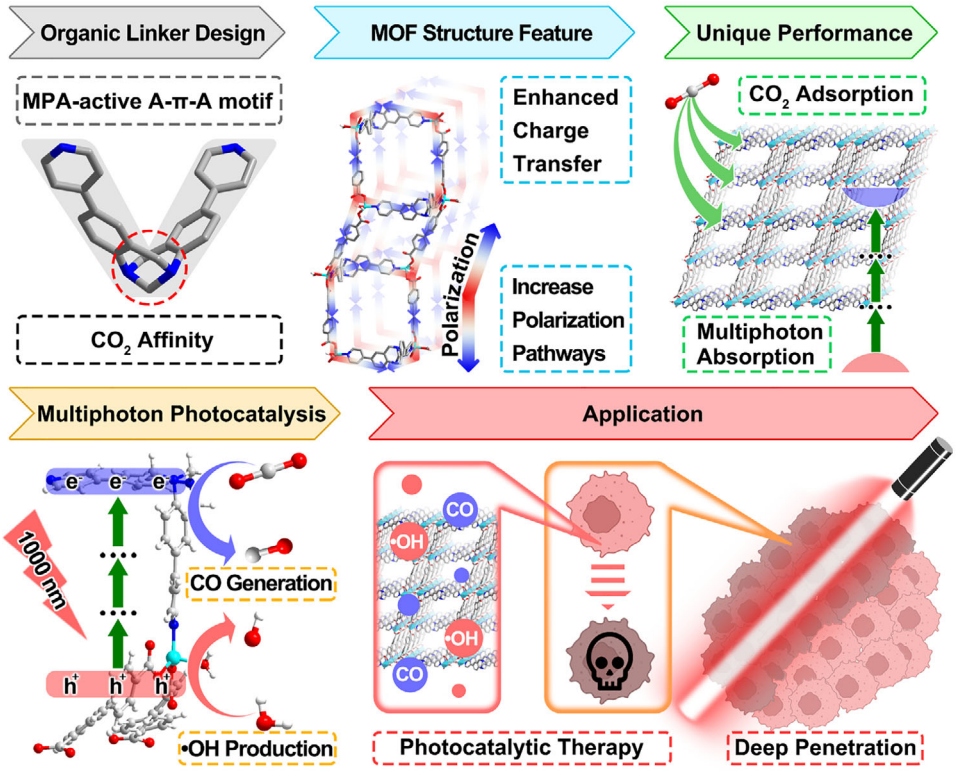

SCHEME 1 | Schematic illustration of a multiphoton absorbing MOF system enabling NIR-driven photocatalytic CO_2 reduction and H_2O oxidation for therapeutic applications.

systems are activated by visible-light, which suffers from poor tissue penetration, severely restricting their applicability for deep-seated tumors. Moreover, many photocatalytic materials exhibit insufficient CO_2 adsorption capacity and poor catalytic activity, resulting in low CO yields [17–19]. Given the limited endogenous CO_2 concentration in tumors, many such systems often require external CO_2 supplementation, complicating therapeutic delivery.

Multiphoton photocatalysis offers a transformative solution to these challenges, enabling both deep tissue penetration and enhanced photocatalytic performance [20–24]. By harnessing multiple NIR photons as the excitation source, multiphoton systems enable effective treatment of deep-seated tumors while overcoming the inherent limitations of traditional NIR photocatalysts, including low redox potentials and rapid charge recombination. The exceptional potential of this system can be further amplified when combined with metal-organic frameworks (MOFs), which possess high surface areas, tunable pore structures, and exceptional CO_2 capture capabilities [25–30]. The precisely engineered porous architecture of MOFs concentrate CO_2 molecules around catalytic sites, creating an optimal microenvironment for efficient photocatalytic CO_2 conversion [31–34]. This synergy between multiphoton excitation and MOF-based catalysis lays the foundation for a highly promising platform for photocatalytic CO therapy, offering both spatial precision and robust therapeutic efficacy.

Bearing the above points in mind, we herein report the design and synthesis of a novel Zn-based MOF, namely ZnTBH, for the first time to enable effective NIR-mediated CO therapy through multiphoton photocatalytic CO_2 reduction (Scheme 1). This framework is constructed by coordinating Zn^{2+} nodes with biphenyl-4,4'-dicarboxylic acid (BPDC) and a CO_2-philic TB [35–37] derivative (TB-bpy) as linkers. Upon photoexcitation, photogenerated electrons are primarily located on TB-bpy, while holes are accumulated on BPDC, thereby driving efficient CO_2 reduction as well as H_2O oxidation. Moreover, the unique coordination environment and hydrogen bonding within ZnTBH enhance charge transfer and increase polarization pathways, collectively enabling efficient multiphoton absorption (MPA) upon NIR light excitation. To further improve its therapeutic performance and biocompatibility, we engineer liposome-modified ZnTBH nanoparticles (nTBHL NPs) that maintain excellent aqueous stability while serving as effective photocatalytic agents. Upon 1000 nm irradiation, nTBHL NPs achieve efficient conversion of dilute CO_2 to CO for gas therapy, while simultaneously oxidizing H_2O to generate hydroxyl radicals (•OH) for photodynamic therapy (PDT), overcoming the critical challenge of utilizing physiologically relevant CO_2 concentrations in cancer treatment. This dual-modality NIR-activated multiphoton system demonstrates significant potential for next-generation MOF-based cancer therapies, particularly for treating deep-seated tumors where conventional phototherapies fall short.

2 | Results and Discussion

ZnTBH, $(Zn(TB\text{-}bpy)_1(BPDC)_2 \cdot H_2O)$, has been successfully synthesized via a solvothermal reaction (see Supporting Information) involving 2,8-di(pyridin-4-yl)-6H,12H-5,11-methanodibenzo-[b,f][1,5] diazocine (TB-bpy, see Figures S1, S2, and Table S1 for

15213773, 2026, 10, Downloaded from https://onlinelibrary.wiley.com/doi/10.1002/anie.202524756 by University Of Science, Wiley Online Library on [04/03/2026]. See the Terms and Conditions (https://onlinelibrary.wiley.com/terms-and-conditions) on Wiley Online Library for rules of use; OA articles are governed by the applicable Creative Commons License

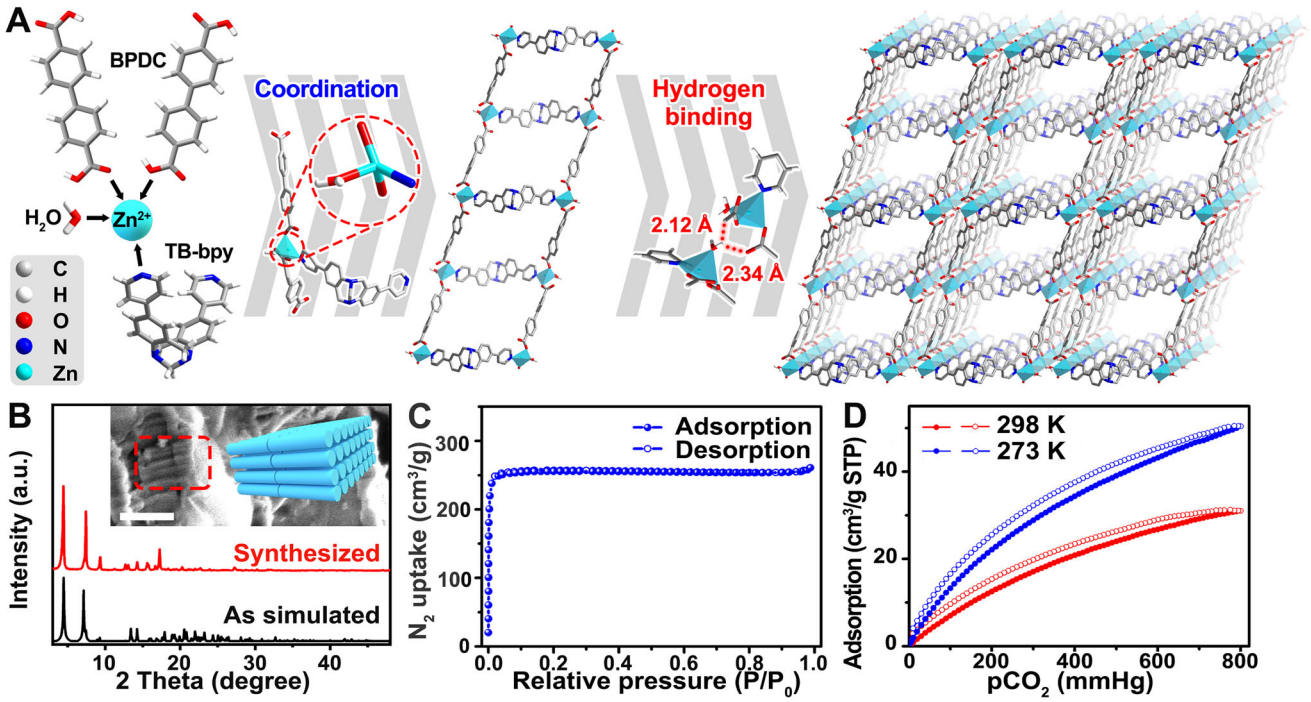

FIGURE 1 | (A) The assembly process of ZnTBH. (B) PXRD pattern simulated from the single-crystal structure and obtained experimentally. The inset images show the corresponding SEM image of ZnTBH (scal bar: 1 μm). (C) N_2 adsorption (solid curve) and desorption (open curve) isotherms of ZnTBH at 77 K. (D) The CO_2 sorption curves of ZnTBH at 298 K and at 273 K (solid: adsorption curve; open: desorption curve).

synthesis details and characterization), BPDC, and $Zn(NO_3)_2 \cdot 6H_2O$. The TB-bpy linker is strategically designed with a V-shaped MPA-active A-π-A motif, where the pyridine groups serve as electron acceptors (A) and the TB moiety acts as a π-bridge. Notably, TB is inherently CO_2-philic, while BPDC is incorporated as an auxiliary ligand to align the polarization vector of ZnTBH and promote directional charge transfer, synergistically enhancing MPA activity.

High-quality bulk single crystals of ZnTBH have been successfully obtained, enabling single-crystal x-ray diffraction analysis (space group C2/c, Table S2). The Zn^{2+} center is four-coordinated with a distorted tetrahedral geometry. Notably, the coordination environments of Zn^{2+} are completed by one N atom from TB-bpy, two O atoms from BPDC, and one O atom from a coordinated water molecule, leaving open coordination sites. Detailed structural analyses reveals that the TB-bpy and BPDC linkers bridge Zn^{2+} nodes to form two-dimensional layers featuring one-dimensional quadrilateral channels along the c-axis. These layers are further assembled into a three-dimensional network via O—H···O hydrogen bonding interactions between the carboxylate groups of BPDC and the Zn-coordinated water molecules, resulting in porous channels measuring about 18.6 Å (Figure 1A). Meanwhile, ZnTBH remains excellent stability in solutions under different conditions (pH = 3–12) during 24 h (Figure S3).

Powder x-ray diffraction (PXRD) analysis confirms that the bulk powder maintains the same crystalline phase as the single crystals, while scanning electron microscopy (SEM) unveil a block-like morphology composed of rod-like crystals (Figures 1B and S4). N_2 adsorption measurements yield a BET surface area of 746 $m^2\ g^{-1}$ at 77 K, corroborating the porosity of ZnTBH (Figure 1C). As shown, in Figure S5, ZnTBH shows a predominant pore size of about 1.1 nm, further supporting its microporous nature. Additionally, ZnTBH exhibits a CO_2 adsorption enthalpy (ΔH) of 22.8 kJ/mol (Figure S6), along with uptake capacities of 50.37 $cm^3\ g^{-1}$ at 273 K and 31.06 $cm^3\ g^{-1}$ at 298 K, demonstrating its intrinsic CO_2 adsorption capacity (Figure 1D).

Motivated by the aforementioned results, the photocatalytic CO_2 reduction ability of ZnTBH is subsequently explored. Before this, the surface of ZnTBH is modified with liposomes (denote as ZnTBHL) to enhance its stability in aqueous photocatalytic systems. As evidenced by Figure S7, successful liposome coating is achieved. Photocatalytic evaluation is conducted owing to the pronounced light absorption of ZnTBHL within the 300–500 nm range (Figure S8). Remarkably, efficient photocatalytic CO_2 reduction is achieved in aqueous medium without requiring additional photosensitizers, sacrificial agents, or noble metal co-catalysts. Under full-spectrum irradiation, ZnTBHL demonstrates a CO production rate of 6.9 μmol $g^{-1}\ h^{-1}$, consistent with the yield determined by the hemoglobin (Hb) assay (Figure S9). Even under a diluted CO_2 atmosphere (5% and 15% CO_2 in N_2), the system maintains considerable photocatalytic activity, achieving CO evolution rates of 0.82 and 5.19 μmol $g^{-1}\ h^{-1}$, respectively. This performance significantly outperforms that of the known visible-light photocatalysts (Figure 2A, Table S3). The origin of CO is further confirmed through isotopic labeling experiments, in which the peak observed at m/z = 29 can be assigned to ^{13}CO, demonstrating that CO_2 serves as the carbon source for the produced CO (Figure S10). Notably, recycling tests reveal negligible activity loss, highlighting exceptional photocatalytic stability (Figure S11). This stability is further verified by PXRD

15213773, 2026, 10, Downloaded from https://onlinelibrary.wiley.com/doi/10.1002/anie.202524756 by University Of Science, Wiley Online Library on [04/03/2026]. See the Terms and Conditions (https://onlinelibrary.wiley.com/terms-and-conditions) on Wiley Online Library for rules of use; OA articles are governed by the applicable Creative Commons License

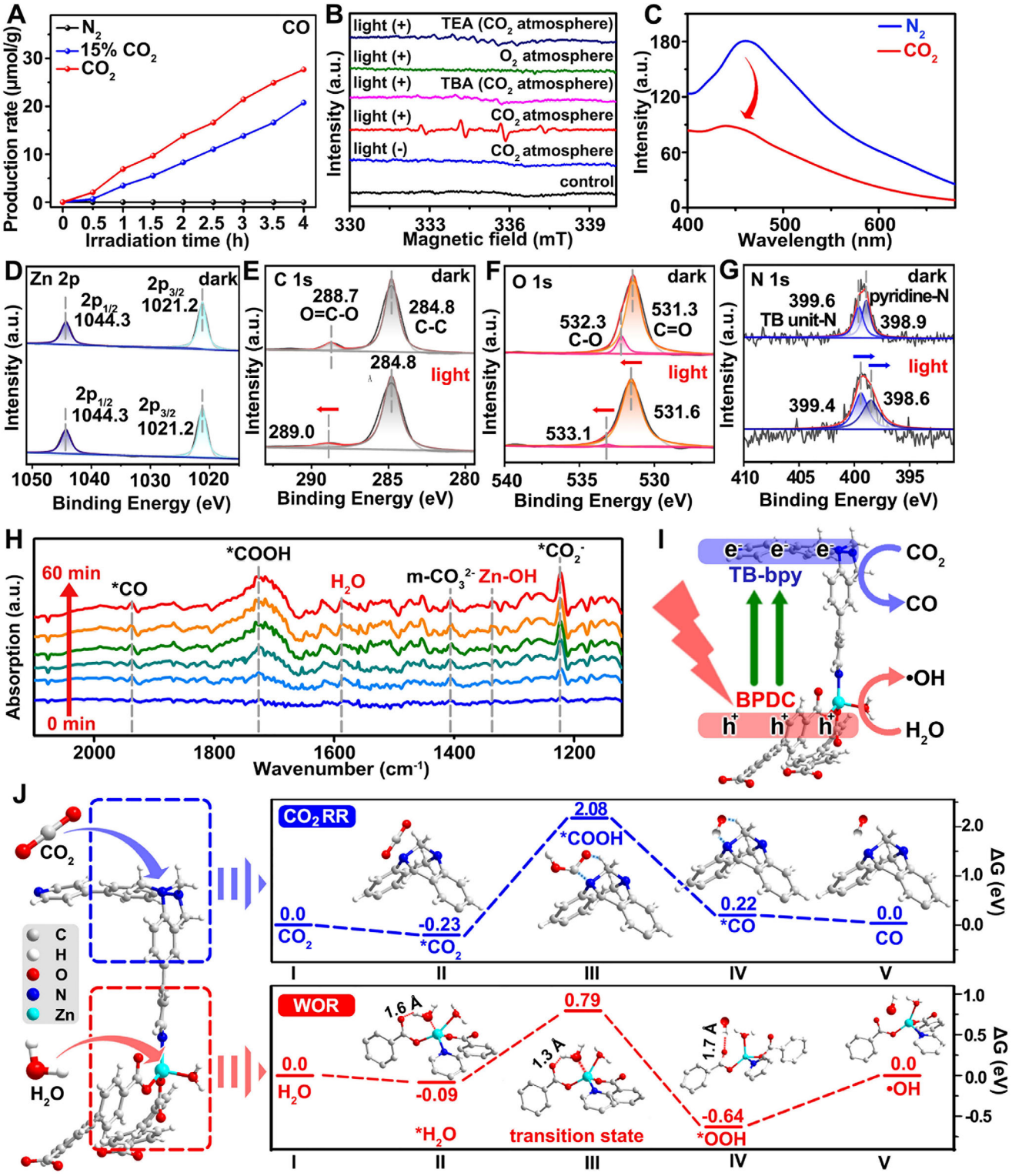

FIGURE 2 | (A) Photocatalytic CO_2 reduction activity over ZnTBHL in different atmosphere under full spectrum irradiation. (B) ESR spectra for the •OH detection in the presence of ZnTBHL under different conditions. (C) The fluorescence spectra of ZnTBHL (100 μg/mL aqueous solution) under N_2 and CO_2 atmospheres, respectively. (D–G) In situ XPS spectra of Zn 2p, C 1s, O 1s, and N 1s of ZnTBH before and after illumination. (H) In situ DRIFTS recording photocatalytic reaction intermediates over ZnTBHL under full-spectrum light irradiation. (I) Schematic diagram of CO and •OH generation of ZnTBHL under light irradiation. (J) Structural models of the photocatalytic reaction pathway in ZnTBH.

15213773, 2026, 10, Downloaded from https://onlinelibrary.wiley.com/doi/10.1002/anie.202524756 by University Of Science, Wiley Online Library on [04/03/2026]. See the Terms and Conditions (https://onlinelibrary.wiley.com/terms-and-conditions) on Wiley Online Library for rules of use; OA articles are governed by the applicable Creative Commons License

analysis and absorption spectra, which confirm retained structural integrity and crystallinity after reaction (Figures S12 and S13).

Furthermore, a mechanistic exploration utilizing electron spin resonance (ESR) spectroscopy with 5,5-dimethyl-1-pyrroline N-oxide (DMPO) as a radical trap furnished direct proof of •OH generation during photocatalysis. As shown in Figure 2B, ZnTBHL can generate •OH in a CO_2 atmosphere under illumination, as confirmed by ESR spectroscopy combined with the •OH scavenger experiment using *tert*-butanol (TBA). Importantly, no •OH signal is detected in an O_2 atmosphere, ruling out the involvement of photogenerated electrons in the formation process. Furthermore, when triethanolamine (TEA) is introduced as a hole scavenger, the •OH signal is almost completely suppressed, providing clear evidence that the generation of •OH proceeds predominantly through a hole-mediated pathway. These results collectively demonstrate that ZnTBHL simultaneously drives CO_2 reduction to CO through photogenerated electrons and water oxidation to •OH via hole-mediated pathways.

Following the experimental confirmation of CO and •OH production, we systematically investigate the photocatalytic mechanism of ZnTBH through a combination of spectroscopic, electrochemical, and computational methods. As shown in Figure S14, compared to its organic linkers (BPDC: 0.44 ns; TB-bpy: 0.53 ns), ZnTBH exhibits a dramatically extended fluorescence lifetime of 2.45 ns, which facilitates the transport and separation of photogenerated charges, thereby enhancing photocatalytic activity [38, 39]. In addition, under a CO_2 atmosphere, the fluorescence intensity of ZnTBH decreases significantly, suggesting efficient electron transfer from photoexcited species to CO_2 molecules (Figure 2C). Then, femtosecond transient absorption spectroscopy is carried out to establish the electron transfer pathway. As presented in Figures S15A, B, ZnTBH exhibits broad positive excited-state signals in the range of 500–720 nm, reflecting the nature of the excited-state species. Furthermore, kinetic fitting at 640 nm reveals a longer lifetime under a CO_2 atmosphere (Figure S15C). This prolonged lifetime suggests the formation of a long-lived charge-separated state resulting from photoinduced charge transfer between ZnTBH and CO_2 [40–43]. Subsequent evidence from Tauc-plot analysis of diffuse reflectance spectra and Mott-Schottky measurements confirm that ZnTBH possesses appropriate band positions for both CO_2 reduction (conduction band at -0.53 V vs. NHE, pH = 7) and H_2O oxidation (valence band at 2.37 V vs. NHE, pH = 7), establishing the thermodynamic feasibility of these photocatalytic conversions (Figure S16).

The in situ x-ray photoelectron spectroscopy (XPS) allows direct elucidation of charge transfer pathways in photocatalysts by monitoring changes in the binding energies of relevant elements. As presented in Figure 2D, the binding energy of Zn 2p remains unchanged before and after illumination. Obviously, under the Xenon lamp irradiation, the binding energy of carboxyl group exhibits a blue shift (Figure 2E,F). Concurrently, the N 1s peak associated with the Tröger's base (TB) unit-N shows a red shift from 399.6 eV in darkness to 399.4 eV under light irradiation (Figure 2G). These results indicate that photogenerated charge transfer occurs from BPDC to TB-bpy within ZnTBH [44–46].

Further, mechanistic insights have been obtained through in situ diffuse reflectance infrared Fourier transform spectroscopy (DRIFTS) under a mixed atmosphere (CO_2 and H_2O), which identify several key reaction intermediates (Figure 2H). The observed peaks at 1223 and 1407 cm^{-1} correspond to $*CO_2^-$ and CO_3^{2-} species, respectively, signaling successful CO_2 activation over the MOF [47, 48]. As the irradiation time under the full- spectrum xenon lamp increased, the signal of the *COOH intermediate at 1721 cm^{-1} gradually increases, providing direct evidence for the CO formation pathway. The vibrational peak observed at 1937 cm^{-1} corresponds to bridge-bound *CO species, which facilitates CO adsorption and generation. Additionally, the H_2O vibrational peak at 1587 cm^{-1} and Zn—H_2O bending vibration at 1334 cm^{-1} are attributed to the unsaturated coordination environment of Zn centers, leading to the adsorption of water molecules and thereby promoting the water oxidation process [49, 50].

Density functional theory calculations complement these experimental findings by revealing that photogenerated holes are primarily located on BPDC while electrons are accumulated on TB-bpy (Figure S17). Analysis of the frontier molecular orbitals by DFT further reveals that the highest occupied molecular orbital (HOMO) and the lowest unoccupied molecular orbital (LUMO) of ZnTBH are spatially separated on different linkers without overlap, indicating a chemically segregated state (Figure S18). These results suggest that a linker-to-linker charge transfer process occurs in ZnTBH, thereby driving the photocatalytic process (Figure 2I) [51, 52]. In addition, DFT calculations reveal that the Zn centers and TB units can adsorb H_2O and CO_2, respectively. The TB units are identified as the active sites for CO_2 reduction following the pathway: $CO_2 \rightarrow *CO_2 \rightarrow *COOH \rightarrow *CO$, with the Gibbs free energy profile (top line in Figure 2J) supporting the thermodynamic feasibility of this process. Simultaneously, the adsorbed H_2O on the open coordination sites of Zn centers forms an O—H···O hydrogen bond (1.70 Å) with a neighboring BPDC carbonyl group. This bond shortens to 1.30 Å at the transition state, facilitating the oxidation process via the formation of an *OOH intermediate. This step is highly favorable, as evidenced by a significant decrease in Gibbs free energy from 0.79 to -0.64 eV, ultimately resulting in the release of a •OH radical (bottom line in Figure 2J) [53, 54]. These comprehensive results demonstrate that, under light irradiation, ZnTBH enables simultaneous CO_2 reduction to CO at the TB-bpy linker through photogenerated electrons, while the BPDC linker drives water oxidation to •OH via hole-mediated mechanisms, demonstrating a synergistic photocatalytic mechanism with significant potential for photocatalytic therapy.

Given the exceptional photocatalytic activity of ZnTBH and the MPA-active motif within its framework, we proceed to evaluate its MPA activity and multiphoton photocatalysis performance. Prior to this evaluation, we successfully synthesize nanoscale ZnTBHL, designated as nTBHL NPs, to facilitate biological studies [55, 56]. The as-prepared nTBHL NPs display a uniform morphology with an average diameter of 120 nm (Figure S19), while maintaining structural integrity, crystallinity, porosity, and a level of catalytic activity comparable to that of pristine ZnTBHL (Figures S20, S21, and Table S4). Notably, nTBHL NPs exhibit excellent colloidal and physiological stability, as evidenced by negligible size variations after a 7 day incubation in both phosphate-buffered saline

15213773, 2026, 10, Downloaded from https://onlinelibrary.wiley.com/doi/10.1002/anie.202524756 by University Of Science, Wiley Online Library on [04/03/2026]. See the Terms and Conditions (https://onlinelibrary.wiley.com/terms-and-conditions) on Wiley Online Library for rules of use; OA articles are governed by the applicable Creative Commons License

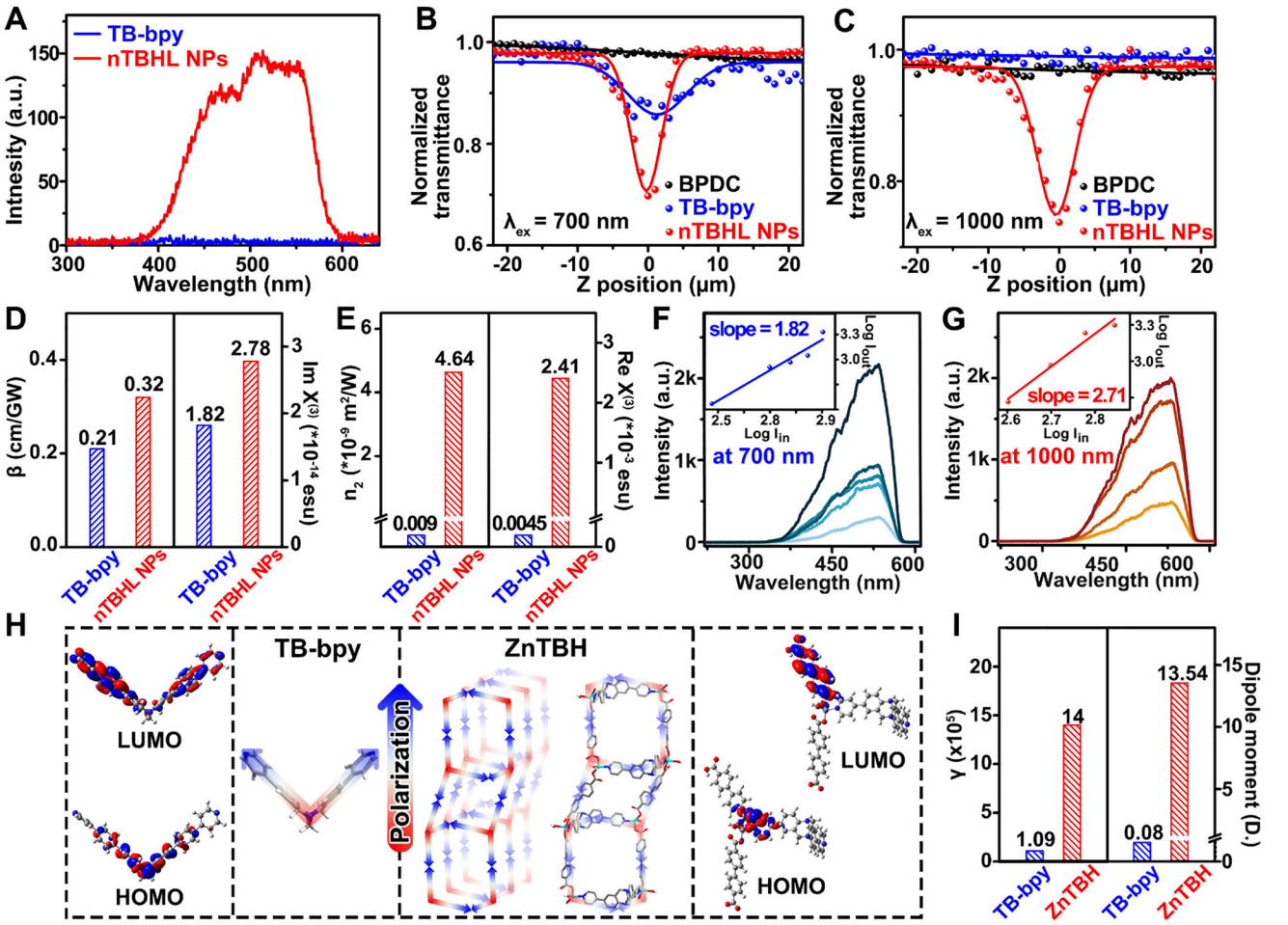

FIGURE 3 | (A) Two-photon excited fluorescence spectra of TB-bpy and nTBHL NPs excited upon 700 nm irradiation. (B) Open aperture Z-scan plots of BPDC, TB-bpy, and nTBHL NPs upon 700 nm irradiation. (C) Open aperture Z-scan plots of BPDC, TB-bpy, and nTBHL NPs upon 1000 nm irradiation. (D) The nonlinear absorption coefficient (β) and imaginary part of third-order susceptibility (Im$\chi^{(3)}$) values of TB-bpy and nTBHL NPs. (E) The nonlinear refractive index (n_2) and real part of third-order susceptibility (Re$\chi^{(3)}$) values of TB-bpy and nTBHL NPs. (F) Two-photon excited fluorescence spectra of nTBHL NPs upon 700 nm irradiation with different input power. (G) Three-photon excited fluorescence spectra of nTBHL NPs upon 1000 nm excitation with different input power. (H) Schematic of the polarization change between TB-bpy and ZnTBH. (I) Comparison of static second hyperpolarizabilities (γ) and dipole moment between TB-bpy and ZnTBH.

(PBS) and serum-containing Dulbecco's Modified Eagle Medium (Figure S22), making them particularly suitable for biological applications. This finding is supported by the PXRD pattern and high resolution-transmission electron microscopy of nTBHL NPs after incubation in PBS solution for 7 days (Figure S23).

To comprehensively characterize the MPA properties of nTBHL NPs and evaluate their potential for photocatalytic therapy, we perform systematic studies. Initial investigations reveal an undetectable up conversion emission signal from TB-bpy (Figure 3A), its MPA behavior is evaluated using the open-aperture Z-scan technique. Quantitative analysis of the log T_0 versus log E plot (where T_0 represents minimum normalized transmittance and E denotes laser pulse energy) at 700 nm excitation yields a slope of 1.33 (n = 2.33) for TB-bpy (Figure S24) [57], confirming its predominant two-photon absorption characteristic due to its A-π-A configuration.

In contrast to TB-bpy, nTBHL NPs demonstrate significantly enhanced reverse saturable absorption at 700 nm (Figure 3B). More importantly, while TB-bpy displays no response at 1000 nm, nTBHL NPs maintain detectable reverse saturable absorption signals under this longer wavelength excitation (Figure 3C). Slope analysis reveals values of 1.1 and 1.62 (n = 2.1 and 2.62) for nTBHL NPs at 700 and 1000 nm excitations, respectively (Figure S25), suggesting the coexistence of both two-photon and three-photon absorption processes. Further quantitative evaluation of nonlinear optical parameters, including the nonlinear absorption coefficient (β), nonlinear refractive index (n_2), and the real and imaginary components of third-order susceptibility (Re $\chi^{(3)}$ and Im $\chi^{(3)}$), showcase the superior MPA performance of nTBHL NPs under 700 nm irradiation. Specifically, nTBHL NPs achieve $\beta = 0.32$ cm/GW, Im$\chi^{(3)} = 2.78 \times 10^{-14}$ esu, $n_2 = 4.64 \times 10^{-9}$ cm^2/W, and Re $\chi^{(3)}$ = 2.41 × 10^{-3} esu (Figure 3D,E), representing the highest nonlinear optical response among all tested samples. Subsequently, we investigate the multiphoton excited fluorescence properties of nTBHL NPs, which exhibit strong upconversion fluorescence under NIR excitation. The slopes of logI_{in} versus logI_{out} for nTBHL NPs are calculated as 1.82 and 2.71 under 700 and 1000 nm, respectively, demonstrating their two- and

15213773, 2026, 10, Downloaded from https://onlinelibrary.wiley.com/doi/10.1002/anie.202524756 by University Of Science, Wiley Online Library on [04/03/2026]. See the Terms and Conditions (https://onlinelibrary.wiley.com/terms-and-conditions) on Wiley Online Library for rules of use; OA articles are governed by the applicable Creative Commons License

three-photon absorption processes. (Figures S26, Figure 3F, and 3G). Quantitative assessment yields an impressive two-photon action cross-section ($\Phi\delta$) of 73.25 GM (where Φ represents quantum yield and δ denotes two-photon absorption cross-section), indicating excellent multiphoton excited fluorescence imaging capability. Furthermore, nTBHL NPs exhibit a substantial three-photon absorption cross-section (δ_{3PA}) of 7.53×10^{-80} cm^6 s^2 $photon^{-2}$, confirming the robust three-photon activity. These exceptional optical properties, combined with the high photostability of nTBHL NPs (Figure S27), establish their great potential as an efficient NIR-driven multiphoton photocatalyst.

To unveil the structural underpinnings behind the enhanced MPA performance in nTBHL NPs compared to TB-bpy, we delve into detailed structure-activity relationship studies. Firstly, the emergence of new charge-transfer states (linker-to-linker charge transfer) resulting from the coordination of Zn centers can yield higher MPA responses than those observed for an uncoordinated linker alone [58, 59]. Secondly, the intricate molecular environment of ZnTBH, characterized by a diverse array of strong and weak forces (including coordination bonds and hydrogen bonding), is poised to positively influence the electron density and polarizability of such systems, consequently impacting MPA performance (Figure 3H) [60–62]. Theoretical calculations further validate these findings, showcasing that ZnTBH exhibits an increased dipole moment and second hyperpolarizability (γ) (Figure 3I). Collectively, the distinctive coordination environment and hydrogen bonding within ZnTBH contributed to enhanced charge transfer and expanded polarization pathways, culminating in the superior MPA and multiphoton excited fluorescence performance of nTBHL NPs (Figures S18 and S28).

Encouraged by these promising outcomes, we delve into investigating the multiphoton photocatalytic CO production capability of nTBHL NPs using the FL-CO probe [63]. Under 1000 nm irradiation, time-dependent fluorescence measurements show a characteristic emission enhancement at 525 nm (Figure S29), providing unambiguous evidence of NIR-driven CO generation. To mimic the conditions of the tumor microenvironment (TME) where CO_2 partial pressure typically reaches around 80 mmHg, we scrutinize the photocatalytic performance of nTBHL NPs under a dilute CO_2 atmosphere (15%). Quantitative analysis employing the Hb assay, which detects CO through the formation of carboxyhemoglobin (HbCO) complexes [64], unveils a notable CO yield of 8.47 μM following 4 min of 1000 nm irradiation, with an apparent quantum yield of 0.101%. Impressively, even under reduced CO_2 concentration (5%), nTBHL NPs maintain a high CO production level of 7 μM (Figures 4A and S30), surpassing the performance of most reported materials (Table S5). Complementary ESR studies substantiate the simultaneous generation of •OH under 1000 nm irradiation (Figure 4B). The robust multiphoton photocatalytic production of both CO and •OH under 1000 nm illumination establishes a strong foundation for developing effective photocatalytic therapeutic approaches.

Afterward, we evaluate the intracellular CO production and •OH generation capabilities of nTBHL NPs upon NIR light irradiation. Significant fluorescence signals from nTBHL NPs in HepG2 cells (Figure S31), confirming successful cellular uptake. As demonstrated in Figure 4C, upon 1000 nm irradiation, nTBHL NPs-treated HepG2 cells exhibit pronounced fluorescence signals from both FL-CO (a CO-specific probe) and hydroxyphenyl fluorescein (HPF, a •OH-sensitive probe), clearly indicating robust intracellular generation of these therapeutic species. Subsequently, the in vitro photocatalytic therapeutic efficacy of nTBHL NPs is evaluated using HepG2 cells stained with calcein acetoxymethyl ester (calcein AM, green fluorescence, indicating live cells) and propidium iodide (PI, red fluorescence, indicating dead cells). Time-dependent experiments show progressive intensification of PI fluorescence with prolonged irradiation (Figure S32), demonstrating the excellent photocatalytic therapeutic performance of nTBHL NPs. These observations are further validated through complementary MTT assay, resazurin cell viability testing, and flow cytometry analyses (Figures S33 and S34).

Given these promising results, we proceed to elucidate the underlying therapeutic mechanism of nTBHL NPs. Building on previous reports highlighting mitochondria as primary targets of CO therapy, we first investigate mitochondrial dysfunction using JC-1 staining to monitor changes in membrane potential ($\Delta\psi_m$). Comparative analysis of J-monomers (green fluorescence, predominantly distributed in the cytosol) and J-aggregates (red fluorescence, localized in the intact mitochondrial membrane) reveal a marked increase in green fluorescence accompanied by decreased red signals relative to controls (Figure 4D). In addition, we have performed bio-transmission electron microscopy of HepG2 cells treated with nTBHL NPs under NIR laser irradiation. As shown in Figure S35, compared with the control group, cells expose to nTBHL NPs followed by NIR irradiation exhibit marked morphological alterations in mitochondria, including reduced mitochondrial size, disappearance of cristae, membrane rupture and cavitation. These observations confirm that nTBHL NPs induce mitochondrial damage upon light irradiation [65–67]. Further using annexin V-FITC/PI staining confirms that nTBHL NPs induces cancer cell apoptosis through mitochondrial impairment (Figure S36). Mechanistic studies show significant NIR light-dependent reduction in cellular ATP levels (Figure 4E), reinforcing the mitochondrial dysfunction hypothesis. To gain deeper insights into this process, a western blot assay is conducted to examine proteins associated with mitochondrial dysfunction, including Akt-1, Nrf-2, and HMOX-1. Compared to the control group, significantly elevated protein expression levels are observed in HepG2 cells treated with nTBHL NPs under 1000 nm irradiation (Figure 4F) [68]. Collectively, these findings establish that nTBHL NPs exert potent anticancer effects through a mitochondria-targeted mechanism involving CO/•OH generation, $\Delta\psi_m$ depolarization, ATP depletion, and activation of mitochondrial stress pathways. These results position nTBHL NPs as promising candidates for multiphoton photocatalytic cancer therapy.

Note that mostly photocatalytic therapeutic systems suffer from limited tissue penetration, severely hindering their application for deep-seated tumors. Thanks to the excellent multiphoton photocatalytic activity of nTBHL NPs under NIR light irradiation, its tissue penetration and deep-seated tumor treatment efficacy are preliminarily evaluated. Remarkably, multiphoton excitation fluorescence imaging of nTBHL NPs in both cellular and tissue samples reveal outstanding performance in NIR-activated three-photon excited fluorescence imaging. Compared to conventional

15213773, 2026, 10, Downloaded from https://onlinelibrary.wiley.com/doi/10.1002/anie.202524756 by University Of Science, Wiley Online Library on [04/03/2026]. See the Terms and Conditions (https://onlinelibrary.wiley.com/terms-and-conditions) on Wiley Online Library for rules of use; OA articles are governed by the applicable Creative Commons License

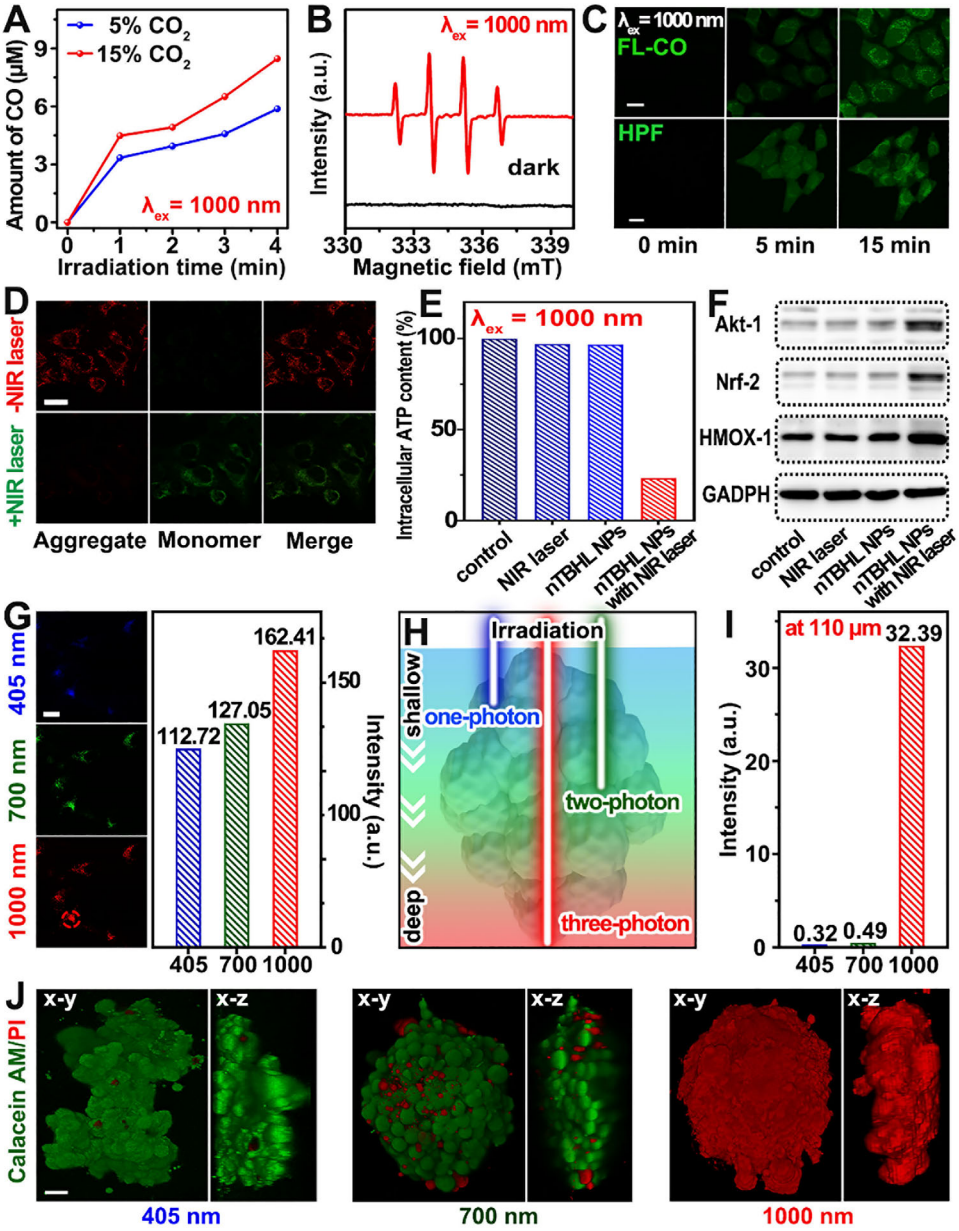

FIGURE 4 | (A) The quantitative content of CO release treated with nTBHL NPs (100 μg/mL) by NIR-mediated photocatalysis (1000 nm, 1 W cm^{-2}) under 5% and 15% CO_2. (B) ESR spectra of nTBHL NPs under 15% CO_2 in the presence of DMPO upon 1000 nm irradiation. (C) Fluorescence detection of CO (FL-CO probe, 0.1 μM) and •OH (HPF probe, 0.1 μM) in nTBHL NPs-treated (100 μg/mL) HepG2 cells upon 1000 nm irradiation. Scale bar: 20 μm. (D) CLSM images of nTBHL NPs-treated (100 μg/mL) HepG2 cells stained with JC-10 (mitochondrial potential probe; λ_{ex} = 1000 nm). Scale bar: 20 μm. (E) The intracellular ATP levels in HepG2 cells incubated with nTBHL NPs upon different treatments (λ_{ex} = 1000 nm). (F) Western blot analysis of Akt-1, Nrf-2, HMOX-1 protein levels in HepG2 cells upon different treatments (λ_{ex} = 1000 nm). (G) One-/two-/three-photon excited fluorescence intensity along the red circle. (H) Schematic diagram of One-/two-/three-photon penetration depth images of HepG2 MCSs treatment with nTBHL NPs (100 μg/mL) upon the irradiation of 405, 700, and 1000 nm. (I) Fluorescence intensity of tissue section at 110 μm (λ_{ex} = 405, 700, and 1000 nm). (J) HepG2 MCSs incubated with nTBHL NPs and calcein AM /PI. HepG2 MCSs were irradiated by 405, 700, and 1000 nm laser (Scale bar: 50 μm).

one-photon and two-photon excited fluorescence imaging, three-photon excited fluorescence imaging of nTBHL NPs exhibits a dramatic enhancement in fluorescence intensity, superior spatial resolution, and significantly deeper tissue penetration (Figures 4G–I, S37, and S38).

Moreover, the therapeutic potential of nTBHL NPs in deep-seated tumors is assessed using HepG2 3D multicellular spheroids (MCSs). Following nTBHL NPs treatment and calcein AM/PI staining, MCSs irradiated with a 1000 nm laser display a time-dependent increase in PI fluorescence (red, dead cells), confirming progressive cell death (Figure 4J). Strikingly, under 1000 nm excitation, strong PI fluorescence is detected not only at the periphery but also in the core region of the tumor spheroids, demonstrating effective deep tumor penetration and treatment efficacy. These findings collectively highlight the robust multiphoton photocatalytic therapeutic potential of nTBHL NPs, particularly their ability to overcome the penetration limitations

15213773, 2026, 10, Downloaded from https://onlinelibrary.wiley.com/doi/10.1002/anie.202524756 by University Of Science, Wiley Online Library on [04/03/2026]. See the Terms and Conditions (https://onlinelibrary.wiley.com/terms-and-conditions) on Wiley Online Library for rules of use; OA articles are governed by the applicable Creative Commons License

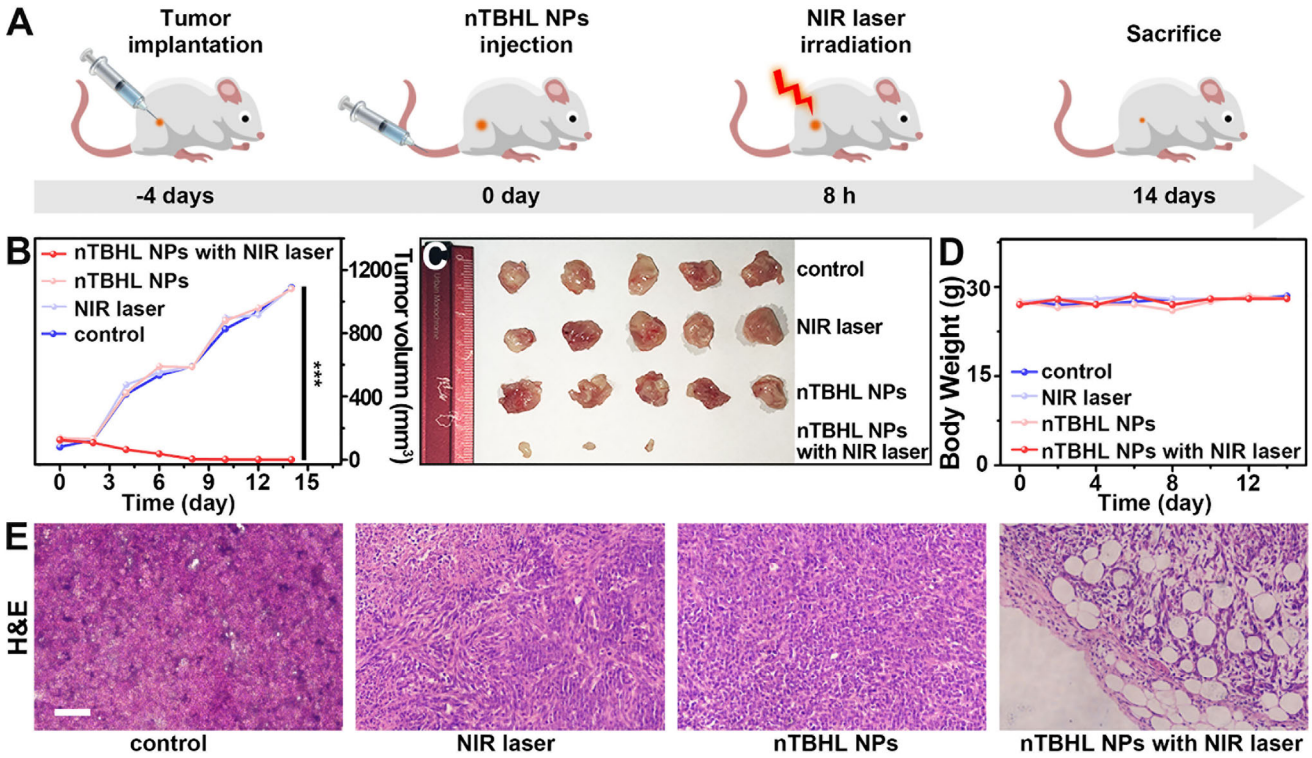

FIGURE 5 | (A) Schematic representation of the development and treatment protocol for the H22 subcutaneous tumor-bearing female ICR mouse model. (B) Tumor volume curves of the different groups (λ_{ex} = 1000 nm). (C) Digital images of excised tumors after 14 days of various treatments (λ_{ex} = 1000 nm). (D) Body weight curves of the various treatment groups (λ_{ex} = 1000 nm). (E) H&E-stained sections of tumors from distinct treatment groups (scale bar: 500 μm, λ_{ex} = 1000 nm). The data are shown as mean values ± standard deviations (n = 5). Statistical analysis was conducted with unpaired t-test analysis (ns, not significant, *p < 0.05, **p < 0.01, and ***p < 0.001).

of conventional phototherapy and effectively treat deep-seated tumors via NIR light activation.

To evidence the feasibility of nTBHL NPs in vivo, we then evaluate their performance on a H22 tumor-bearing mice model. Initial biosafety evaluation reveals excellent hemocompatibility, with nTBHL NPs exhibiting a hemolysis ratio of only 3.9%, well below the 5% safety threshold for intravenous administration (Figure S39). The tumor-targeting capability of nTBHL NPs is confirmed through fluorescence imaging, which shows significant accumulation at the tumor site 24 h post-injection (Figure S40). Pharmacokinetic studies further demonstrate favorable circulation characteristics with a blood half-life of 4.36 h (Figure S41), while blood biochemical analysis reveals no abnormalities in nTBHL NPs-treated mice compared to control (Figure S42). These results underscore that nTBHL NPs exhibit favorable biosafety and efficient accumulation in tumor regions.

Based on these promising results, the anticancer efficacy of nTBHL NPs under NIR irradiation is evaluated in H22 tumor-bearing mice models (Figure 5A). Mice are randomly divided into four treatment groups: (1) PBS control, (2) NIR laser alone, (3) nTBHL NPs alone, and (4) nTBHL NPs with NIR irradiation (1000 nm, 1 W/cm^2). After 14 days of treatment, the nTBHL NPs with NIR irradiation group exhibit remarkable tumor growth suppression, as evidenced by tumor volume measurements and photographic documentation (Figures 5B,C, and S43). The treatment shows excellent safety profiles, with no significant changes in body weight observed throughout the study period (Figure 5D) and no signs of organ toxicity in H&E-stained sections of major organs (Figure S44). Importantly, histopathological analysis of tumor tissues shows significantly reduced cellular proliferation and increased apoptosis in the nTBHL NPs with NIR irradiation compared to controls (Figure 5E). These findings demonstrate that nTBHL NPs-mediated photocatalytic therapy achieves potent antitumor effects under NIR irradiation, while maintaining excellent biosafety.

3 | Conclusion

In summary, we have developed a novel multiphoton photocatalytic system, nTBHL NPs, that enables NIR-mediated synergistic cancer therapy through simultaneous CO generation and ROS production. This innovative system overcomes the critical challenges of deep-tissue penetration and controlled CO release in solid tumors through its unique multiphoton photocatalytic properties. Under NIR irradiation, nTBHL NPs achieve concurrent CO_2 photoreduction to CO (mediated by photogenerated electrons) and water photooxidation to •OH (via hole-driven pathways), creating a potent therapeutic combination. Comprehensive theoretical calculations have elucidated the underlying MPA characteristics and photocatalytic mechanisms, revealing how the distinctive coordination environment and hydrogen bonding network within the MOF framework facilitate enhanced

15213773, 2026, 10, Downloaded from https://onlinelibrary.wiley.com/doi/10.1002/anie.202524756 by University Of Science, Wiley Online Library on [04/03/2026]. See the Terms and Conditions (https://onlinelibrary.wiley.com/terms-and-conditions) on Wiley Online Library for rules of use; OA articles are governed by the applicable Creative Commons License

charge transfer and increased polarization pathways. These features collectively enable efficient three-photon absorption at 1000 nm excitation, with the TB units serving as active sites for CO_2 reduction to CO while the photogenerated holes localize on BPDC catalyze water oxidation to •OH. In vivo evaluations confirm the excellent tumor-targeting capability of this system, significant tumor growth suppression, and potent apoptosis induction, all achieved with minimal systemic toxicity. The combination of favorable biosafety, selective tumor accumulation, and efficient NIR-triggered CO/•OH generation establishes nTBHL NPs as highly promising platforms for NIR-driven photocatalytic cancer therapy, offering a transformative approach for treating deep-seated tumors.

Acknowledgments

This work is supported by the National Key Research and Development Program of China (2021YFA1500400), the National Natural Science Foundation of China (U22A20401, 22331009, 22302147, W2512006, 22171001, 22475001, and 22305001), the Natural Science Foundation of Anhui Province (2408085Y010), and the Key Project of Natural Science Foundation of Anhui Province (2508085ZD002).

Conflicts of Interest

The authors declare no conflict of interest.

Data Availability Statement

The data that support the findings of this study are available from the corresponding author upon reasonable request.

References

1. R. Motterlini and L. Otterbein, "The Therapeutic Potential of Carbon Monoxide," *Nature Reviews Drug Discovery* 9 (2010): 728–743, https://doi.org/10.1038/nrd3228.

2. C. Figueiredo-Pereira, D. Dias-Pedroso, N. L. Soares, and H. L. A. Vieira, "CO-mediated Cytoprotection Is Dependent on Cell Metabolism Modulation," *Redox Biology* 32 (2020): 101470, https://doi.org/10.1016/j.redox.2020.101470.

3. L. Otterbein, "Carbon Monoxide: Innovative Anti-inflammatory Properties of Age-Old Gas Molecule," *Antioxidants & Redox Signaling* 4 (2002): 309–319, https://doi.org/10.1089/152308602753666361.

4. B. Wegiel, D. Gallo, E. Csizmadia, et al., "Carbon Monoxide Expedites Metabolic Exhaustion to Inhibit Tumor Growth," *Cancer Research* 73 (2013): 7009–7021, https://doi.org/10.1158/0008-5472.CAN-13-1075.

5. L. Otterbein, F. H. Bach, J. Alam, et al., "Carbon Monoxide Has Anti-inflammatory Effects Involving the Mitogen-activated Protein Kinase Pathway," *Nature Medicine* 6 (2000): 422–428, https://doi.org/10.1038/74680.

6. S. Lee, S.-J. Lee, A. A. Coronata, et al., "Carbon Monoxide Confers Protection in Sepsis by Enhancing Beclin 1-Dependent Autophagy and Phagocytosis," *Antioxidants Redox Signaling* 20 (2014): 432–442, https://doi.org/10.1089/ars.2013.5368.

7. S. R. Oliveira, C. S. F. Queiroga, and H. L. A. Vieira, "Mitochondria and Carbon Monoxide: Cytoprotection and Control of Cell Metabolism—a Role for Ca 2+ ?," *The Journal of Physiology* 594 (2016): 4131–4138, https://doi.org/10.1113/JP270955.

8. C. Taille, J. El-Benna, S. Lanone, J. Boczkowski, and R. Motterlini, "Mitochondrial Respiratory Chain and NAD(P)H Oxidase Are Targets for theAntiproliferative Effect of Carbon Monoxide in Human Airway SmoothMuscle," *Journal of Biological Chemistry* 280 (2005): 25350–25360, https://doi.org/10.1074/jbc.M503512200.

9. J. D. Roderique, C. S. Josef, M. J. Feldman, and B. D. Spiess, "A Modern Literature Review of Carbon Monoxide Poisoning Theories, Therapies, and Potential Targets for Therapy Advancement," *Toxicology* 334 (2015): 45–58, https://doi.org/10.1016/j.tox.2015.05.004.

10. C. C. Romao, W. A. Blattler, J. D. Seixas, and G. J. L. Bernardes, "Developing Drug Molecules for Therapy With Carbon Monoxide," *Chemical Society Reviews* 41 (2012): 3571, https://doi.org/10.1039/c2cs15317c.

11. G. Zhou, Y. Chen, W. Chen, et al., "Renal Clearable Catalytic 2D Au-Porphyrin Coordination Polymer Augmented Photothermal-Gas Synergistic Cancer Therapy," *Small* 19 (2023): 2206749.

12. G. Ma, Q. Ding, Y. Wang, et al., "Precision Photothermal Therapy at Mild Temperature: NIR-II Imaging-Guided, H 2 O 2 -Responsive Stealth Nano bomb," *Advanced Healthcare Materials* 14 (2025): 2402767, https://doi.org/10.1002/adhm.202402767.

13. P. Ghaffari-Bohlouli, H. Jafari, O. V. Okoro, et al., "Gas Therapy: Generating, Delivery, and Biomedical Applications," *Small Methods* 8 (2024): 2301349, https://doi.org/10.1002/smtd.202301349.

14. H. Yan, J. Du, S. Zhu, et al., "Emerging Delivery Strategies of Carbon Monoxide for Therapeutic Applications: From CO Gas to CO Releasing Nanomaterials," *Small* 15 (2019): 1904382.

15. L. Chen, S.-F. Zhou, L. Su, and J. Song, "Gas-Mediated Cancer Bioimaging and Therapy," *ACS Nano* 13 (2019): 10887–10917.

16. D.-W. Zheng, B. Li, C.-X. Li, et al., "Photocatalyzing CO 2 to CO for Enhanced Cancer Therapy," *Advanced Materials* 29 (2017): 1703822, https://doi.org/10.1002/adma.201703822.

17. F. Yang, X. Cao, T. Yang, et al., "H 2 S-Responsive NIR-II Fluorescent Nanozyme That Regulates Tumor Microenvironment for Activatable Synergistic CO Therapy/Catalytic Therapy/Immunotherapy," *Small* 20 (2024): 2402904, https://doi.org/10.1002/smll.202402904.

18. H. Zhang, L. Feng, Y. Wang, et al., "Spontaneously Photocatalytic Nanoplatform for Sensitive Diagnosis and Penetrated Therapy of Cancer," *Analytical Chemistry* 97 (2025): 2809–2818, https://doi.org/10.1021/acs.analchem.4c05185.

19. W. Yu, J. Fu, F. Jia, Q. Jin, Y. Wang, and J. Ji, "Removable Photocatalysis Microneedle Reactor for Carbon Monoxide Delivery to Enhance Chemosensitization," *Nano Letters* 24 (2024): 10024–10031, https://doi.org/10.1021/acs.nanolett.4c01582.

20. Y.-X. Chen, H. Yu, L. Wu, et al., "Unlocking Multi-photon Excited Luminescence in Pyrazolate Trinuclear Gold Clusters for Dynamic Cell Imaging," *Nature Communications* 15 (2024): 7356, https://doi.org/10.1038/s41467-024-51753-4.

21. Z. Qin, Z. She, C. Chen, et al., "Deep Tissue Multi-photon Imaging Using Adaptive Optics With Direct Focus Sensing and Shaping," *Nature Biotechnology* 40 (2022): 1663–1671, https://doi.org/10.1038/s41587-022-01343-w.

22. C. Han, B. K. Kundu, Y. Liang, and Y. Sun, "Near-Infrared Light-Driven Photocatalysis With an Emphasis on Two-Photon Excitation: Concepts, Materials, and Applications," *Advanced Materials* 36 (2024): 2307759, https://doi.org/10.1002/adma.202307759.

23. J. Jr. Fajardo, A. T. Barth, M. Morales, M. K. Takase, J. R. Winkler, and H. B. Gray, "Photoredox Catalysis Mediated by Tungsten(0) Aryliso-cyanides," *Journal of the American Chemical Society* 143 (2021): 19389–19398.

24. X. Lu, X. Yu, B. Li, et al., "Harnessing Metal-Organic Frameworks for NIR-II Light-Driven Multiphoton Photocatalytic Water Splitting in Hydrogen Therapy," *Advancement of Science* 11 (2024): 2405643, https://doi.org/10.1002/advs.202405643.

25. M. Ding, R. W. Flaig, H.-L. Jiang, and O. M. Yaghi, "Carbon Capture and Conversion Using Metal–organic Frameworks and MOF-based Materials," *Chemical Society Reviews* 48 (2019): 2783–2828, https://doi.org/10.1039/C8CS00829A.

15213773, 2026, 10, Downloaded from https://onlinelibrary.wiley.com/doi/10.1002/anie.202524756 by University Of Science, Wiley Online Library on [04/03/2026]. See the Terms and Conditions (https://onlinelibrary.wiley.com/terms-and-conditions) on Wiley Online Library for rules of use; OA articles are governed by the applicable Creative Commons License

26. D. Li, M. Kassymova, X. Cai, S.-Q. Zang, and H.-L. Jiang, "Photocatalytic CO2 Reduction Over Metal-organic Framework-based Materials," *Coordination Chemistry Reviews* 412 (2020): 213262, https://doi.org/10.1016/j.ccr.2020.213262.

27. P. Gao, Y. Chen, W. Pan, N. Li, Z. Liu, and B. Tang, "Antitumor Agents Based on Metal–Organic Frameworks," *Angewandte Chemie International Edition* 60 (2021): 16763–16776, https://doi.org/10.1002/anie.202102574.

28. B. Achenbach, A. Yurdusen, N. Stock, G. Maurin, and C. Serre, "Synthetic Aspects and Characterization Needs in MOF Chemistry—From Discovery to Applications," *Advanced Materials* 37 (2025): 2411359, https://doi.org/10.1002/adma.202411359.

29. Y. Liu, L. Wang, T. Zhang, et al., "Tumor Microenvironment-Regulating Two-Photon Probe Based on Bimetallic Post-Coordinated MOF Facilitating the Dual-Modal and Deep Imaging-Guided Synergistic Therapies," *ACS Applied Materials & Interfaces* 16 (2024): 12289–12301, https://doi.org/10.1021/acsami.3c18990.

30. B. Chen, D. Fan, R. V. Pinto, et al., "A Scalable Robust Microporous Al-MOF for Post-Combustion Carbon Capture," *Advancement of Science* 11 (2024): 2401070, https://doi.org/10.1002/advs.202401070.

31. S. Guo, L.-H. Kong, P. Wang, S. Yao, T.-B. Lu, and Z.-M. Zhang, "Switching Excited State Distribution of Metal–Organic Framework for Dramatically Boosting Photocatalysis," *Angewandte Chemie International Edition* 61 (2022): e202206193, https://doi.org/10.1002/anie.202206193.

32. Y.-F. Liu, H. He, L. Gao, et al., "Chemical and Mechanical Modifications of Flexible Metal–organic Frameworks for Enhancing Photocatalysis," *Chemical Science* 16 (2025): 14995–15003, https://doi.org/10.1039/D5SC02797G.

33. K. Sun, Y. Qian, and H.-L. Jiang, "Metal-Organic Frameworks for Photocatalytic Water Splitting and CO_2 Reduction," *Angewandte Chemie International Edition* 62 (2023): e202217565.

34. Y.-T. Zheng, S. Li, N.-Y. Huang, X. Li, and Q. Xu, "Recent Advances in Metal–organic Framework-derived Materials for Electrocatalytic and Photocatalytic CO2 Reduction," *Coordination Chemistry Reviews* 510 (2024): 215858, https://doi.org/10.1016/j.ccr.2024.215858.

35. Z. Tang, S. Xu, N. Yin, et al., "Reaction Site Designation by Intramolecular Electric Field in Tröger's-Base-Derived Conjugated Microporous Polymer for near-Unity Selectivity of CO 2 Photoconversion," *Advanced Materials* 35 (2023): 2210693, https://doi.org/10.1002/adma.202210693.

36. X. Chen, Y. Fan, L. Wu, et al., "Ultra-selective Molecular-sieving Gas Separation Membranes Enabled by Multi-covalent-crosslinking of Microporous Polymer Blends," *Nature Communications* 12 (2021): 6140, https://doi.org/10.1038/s41467-021-26379-5.

37. X. Zhu, C.-L. Do-Thanh, C. R. Murdock, et al., "Efficient CO 2 Capture by a 3D Porous Polymer Derived From Tröger's Base," *ACS Macro Letters* 2 (2013): 660–663, https://doi.org/10.1021/mz4003485.

38. Q. Zhang, H. Che, H. Yang, B. Liu, and Y. Ao, "Tandem Proton Transfer in Carboxylated Supramolecular Polymer for Highly Efficient Overall Photosynthesis of Hydrogen Peroxide," *Angewandte Chemie International Edition* 63 (2024): e202409328, https://doi.org/10.1002/anie.202409328.

39. X. Chi, Z. Zhang, M. Li, et al., "Vinylene-Linking of Polycyclic Aromatic Hydrocarbons to π-Extended Two-Dimensional Covalent Organic Framework Photocatalyst for H_2O_2 Synthesis," *Angewandte Chemie International Edition* 64 (2025): e202418895.

40. B. Han, H. He, J. Liu, et al., "Ketyl Radical-mediated Exfoliation and Electron Storage for Solar Hydrogen Peroxide Production," *Nature Communications* 16 (2025): 11046, https://doi.org/10.1038/s41467-025-66852-z.

41. R. Liu, Y. Chen, H. Yu, et al., "Linkage-engineered Donor–acceptor Covalent Organic Frameworks for Optimal Photosynthesis of Hydrogen Peroxide From Water and Air," *Nature Catalysis* 7 (2024): 195–206, https://doi.org/10.1038/s41929-023-01102-3.

42. C. Liu, X. Liu, B. Chen, et al., "Squaric Acid-based Zwitterionic Covalent Organic Framework Induces Triple Synergy for Boosted Hydrogen Peroxide Photosynthesis," *Nature Communications* 16 (2025): 8941, https://doi.org/10.1038/s41467-025-63997-9.

43. A. Wang, M. Du, J. Ni, et al., "Enhanced and Synergistic Catalytic Activation by Photoexcitation Driven S–Scheme Heterojunction Hydrogel Interface Electric Field," *Nature Communications* 14 (2023): 6733, https://doi.org/10.1038/s41467-023-42542-6.

44. L. Wang, Y. Li, Y. Ai, et al., "Tracking Heterogeneous Interface Charge Reverse Separation in SrTiO 3 /NiO/NiS Nanofibers With in Situ Irradiation XPS," *Advanced Functional Materials* 33 (2023): 2306466, https://doi.org/10.1002/adfm.202306466.

45. R. Sun, Z. Zhu, N. Tian, Y. Zhang, and H. Huang, "Hydrogen Bonds and in Situ Photoinduced Metallic Bi^0/Ni^0 Accelerating Z-Scheme Charge Transfer of BiOBr@NiFe-LDH for Highly Efficient Photocatalysis," *Angewandte Chemie International Edition* 63 (2024): e202408862.

46. Q.-M. Sun, J.-J. Xu, F.-F. Tao, et al., "Boosted Inner Surface Charge Transfer in Perovskite Nanodots@Mesoporous Titania Frameworks for Efficient and Selective Photocatalytic CO 2 Reduction to Methane," *Angewandte Chemie International Edition* 134 (2022): e202200872, https://doi.org/10.1002/ange.202200872.

47. N. Dai, Y. Qian, D. Wang, et al., "Regulation of Coordinating Anions Around Single Co(II) Sites in a Covalent Organic Framework for Boosting CO 2 Photoreduction," *Precision in Chemistry* 2 (2024): 600–609, https://doi.org/10.1021/prechem.4c00058.

48. N. Li, X.-P. Zhai, B. Ma, et al., "Highly Selective Photocatalytic CO 2 Reduction via a Lead-free Perovskite/MOF Catalyst," *Journal of Materials Chemistry A* 11 (2023): 4020–4029, https://doi.org/10.1039/D2TA09777J.

49. Z. Teng, H. Yang, Q. Zhang, et al., "Atomically Dispersed Low-valent Au Boosts Photocatalytic Hydroxyl Radical Production," *Nature Chemistry* 16 (2024): 1250–1260, https://doi.org/10.1038/s41557-024-01553-6.

50. M. Jiang, J. Li, X. Wan, et al., "Floatable Organic-inorganic Hybrid-TiO2 Unlocks Superoxide Radicals for Plastic Photoreforming in Neutral Solution," *Nature Communications* 16 (2025): 4136, https://doi.org/10.1038/s41467-025-59467-x.

51. K. Sun, Y. Huang, F. Sun, et al., "Dynamic Structural Twist in Metal–organic Frameworks Enhances Solar Overall Water Splitting," *Nature Chemistry* 16 (2024): 1638–1646, https://doi.org/10.1038/s41557-024-01599-6.

52. G. Wang, Q. Sun, Y. Liu, et al., "A Bismuth-Based Metal–Organic Framework as an Efficient Visible-Light-Driven Photocatalyst," *Chemistry: A European Journal* 21 (2015): 2364–2367, https://doi.org/10.1002/chem.201405047.

53. T. He, H. Tang, J. Wu, et al., "A Metal-free Cascaded Process for Efficient H2O2 Photoproduction Using Conjugated Carbonyl Sites," *Nature Communications* 15 (2024): 7833, https://doi.org/10.1038/s41467-024-52162-3.

54. Q. Wu, H. Zou, X. Mao, et al., "Unveiling the Dynamic Active Site of Defective Carbon-based Electrocatalysts for Hydrogen Peroxide Production," *Nature Communications* 14 (2023): 6275, https://doi.org/10.1038/s41467-023-41947-7.

55. M. Cano-Sarabia, F. Aydin, L. Meng, et al., "Lipid/ZIF-8 Biocomposites Based on Liposomes or Vesicles: In Situ Formation, and Preliminary Evaluation as Delivery Vehicles for Hydrophobic Drugs," *Small* 21 (2025): 2407051, https://doi.org/10.1002/smll.202407051.

56. R. Li, W. Zhao, Z. Han, et al., "Self-Cascade Nanozyme Reactor as a Cuproptosis Inducer Synergistic Inhibition of Cellular Respiration Boosting Radioimmunotherapy," *Small* 20 (2024): 2306263, https://doi.org/10.1002/smll.202306263.

57. Y. Sun, H. Li, X. Gao, Z. Yu, Z. Huang, and C. Zhang, "Superb Nonlinear Absorption of Triphenylene-Based Metal–Organic Frameworks Associated With Abundant Metal D Electrons," *Advanced Optical Materials* 9 (2021): 2100622, https://doi.org/10.1002/adom.202100622.

15213773, 2026, 10, Downloaded from https://onlinelibrary.wiley.com/doi/10.1002/anie.202524756 by University Of Science, Wiley Online Library on [04/03/2026]. See the Terms and Conditions (https://onlinelibrary.wiley.com/terms-and-conditions) on Wiley Online Library for rules of use; OA articles are governed by the applicable Creative Commons License

58. H. He, J. Li, J. Zhuang, et al., "Boosting One- and Two-Photon Excited Fluorescence of Interpenetrated Tetraphenylethene-Based Metal–Organic Frameworks (TPE-MOFs) by Linker Installation," *Angewandte Chemie International Edition* 64 (2025): e202420912, https://doi.org/10.1002/anie.202420912.

59. R. Medishetty, J. K. Zareba, D. Mayer, M. Samoc´, and R. A. Fischer, "Nonlinear Optical Properties, Upconversion and Lasing in Metal–organic Frameworks," *Chemical Society Reviews* 46 (2017): 4976–5004, https://doi.org/10.1039/C7CS00162B.

60. G. S. He, L.-S. Tan, Q. Zheng, and P. N. Prasad, "Multiphoton Absorbing Materials: Molecular Designs, Characterizations, and Applications," *Chemical Reviews* 108 (2008): 1245–1330, https://doi.org/10.1021/cr050054x.

61. M. Drobizhev, A. Karotki, A. Rebane, and C. W. Spangler, "Dendrimer Molecules With Record Large Two-photon Absorption Cross Section," *Optics Letters* 26 (2001): 1081, https://doi.org/10.1364/OL.26.001081.

62. P. Norman and Y. Luo, "Large Two-photon Absorption Cross Sections in Two-dimensional, Charge-transfer, Cumulene-containing Aromatic Molecules," *Journal of Chemical Physics* 111 (1999): 7758–7765, https://doi.org/10.1063/1.480111.

63. S. Feng, D. Liu, W. Feng, and G. Feng, "Allyl Fluorescein Ethers as Promising Fluorescent Probes for Carbon Monoxide Imaging in Living Cells," *Analytical Chemistry* 89 (2017): 3754–3760, https://doi.org/10.1021/acs.analchem.7b00135.

64. T. Zhang, Q. Zheng, J. Huang, and X. Li, "CoOx-Caged Metal-Organic Frameworks for Sonocatalyzing CO 2 to Co for Ultrasound-Assisted Chemodynamic-Gas Cancer Therapy," *Advanced Functional Materials* 34 (2024): 2311029, https://doi.org/10.1002/adfm.202311029.

65. G. Shi, Y. Zhang, W. Wang, et al., "Controlled Synthesis of the FeB Nanometallic Glasses With Stronger Electron Donating Capability to Activate Molecular Oxygen for the Enhanced Ferroptosis Therapy," *Advanced Healthcare Materials* 14 (2025): 2403582, https://doi.org/10.1002/adhm.202403582.

66. Y. An, M. Li, Q. Bai, et al., "A Mitochondrial DNA-Releasing Photosensitizer Potentiates Innate Immunity for Tumor Eradication and Prevention," *Aggregate* 6 (2025): e70194, https://doi.org/10.1002/agt2.70194.

67. H. Du, Z. Li, S.-T. Fu, et al., "Mitochondria-Targeted Dual-Ion Perturbator Amplifies Cuproptosis for Enhanced Melanoma Immunotherapy and Accelerated Postoperative Wound Healing," *ACS Nano* 19 (2025): 37544–37560, https://doi.org/10.1021/acsnano.5c05965.

68. W.-X. Ren, H. Yu, C.-Y. Li, et al., "Engineering a Multifunctional Core-shell Structured Cascade Nanoreactor for Augmented and Synergistic Carbon Monoxide Oncotherapy," *Science China Materials* 68 (2025): 1570–1580, https://doi.org/10.1007/s40843-024-3281-x.

Supporting Information

Additional supporting information can be found online in the Supporting Information section.

Supporting File 1: anie71328-sup-0001-SuppMat.docx.

Supporting File 2: anie71328-sup-0002-Data.zip.

15213773, 2026, 10, Downloaded from https://onlinelibrary.wiley.com/doi/10.1002/anie.202524756 by University Of Science, Wiley Online Library on [04/03/2026]. See the Terms and Conditions (https://onlinelibrary.wiley.com/terms-and-conditions) on Wiley Online Library for rules of use; OA articles are governed by the applicable Creative Commons License